

Supplementary information for:

Exciton ionization induced by intersubband absorption in non-polar ZnO/ZnMgO quantum wells at room temperature.

A. Jollivet¹, P. Quach¹, M. Tchernycheva¹, R. Ferreira², E. Di Russo³, L. Rigutti³, B. Vinter⁴, N. le Biavan⁴, D. Lefebvre⁴, M. Hugues⁴, J-M. Chauveau⁴, F. H. Julien¹

¹ Centre de Nanosciences et de Nanotechnologies, CNRS, Université Paris-Saclay, 91120 Palaiseau, France.

² Laboratoire de Physique de l'Ecole Normale Supérieure, ENS, Université PSL, CNRS, Sorbonne Université, Université de Paris, F-75005 Paris, France

³ Normandie Univ., UNIROUEN, INSA Rouen, CNRS, Groupe de Physique des Matériaux, 76000 Rouen, France.

⁴ Université Côte d'Azur, CNRS, CRHEA, Valbonne, France

Corresponding author: arnaud.jollivet@c2n.upsaclay.fr

A) Effective mass parameters:

The parameters used in Nextnano calculations are listed in the following table.

Parameter	ZnO	MgO	Unit
A	3.246 [1]	3.221 [2]	Å
C	5.213 [1]	5.040 [2]	Å
c ₁₁	238 [2]	205 [2]	GPa
c ₁₂	106 [2]	80 [2]	GPa
c ₁₃	84 [2]	88 [2]	GPa
c ₃₃	176 [2]	222 [2]	GPa
c ₄₄	58 [2]	60 [2]	GPa
E _g	3.442 [3]	-	eV
HH (long.)	2.64 [4]	2.77 [5]	m _e
HH (trasv.)	3.13 [4]	1.6 [5]	m _e
CB eff. mass (Γ)	-	0.42 [2]	m _e

Tab. ST1: Main wurtzite parameters for ZnO and MgO materials used in Nextnano simulations. The Nextnano default parameters have been used for ZnO and MgO if they are not reported in this table.

The heterojunction band offset was set to $\Delta E_c/\Delta E_v = 66.5 : 33.5$ [6].

Determination of parameters for Mg_xZn_{1-x}O materials are calculated from bowing equations [7]. All bowing parameters were set to 0.

B) Valence intersubband transitions

The ISB transition measured may not correspond to VB ISB transitions because of three reasons. The first two reasons are a lower VB band offset [6] and a heavier effective mass [2,4,5] compared to the CB values. These two factors involve a redshift of VB ISB transitions compared to the CB ISB transitions, so the discrepancy between our experimental results and

the VB ISB transitions is enlarged. The third factor is the Reststrahlen band [8] preventing most of the transitions to be detectable. The VB ISB transition energies have been simulated using Nextnano software [9] by solving Schrödinger equation with a mass-effective model and are presented and compared to CB ISB transition energies in the Figure S1.

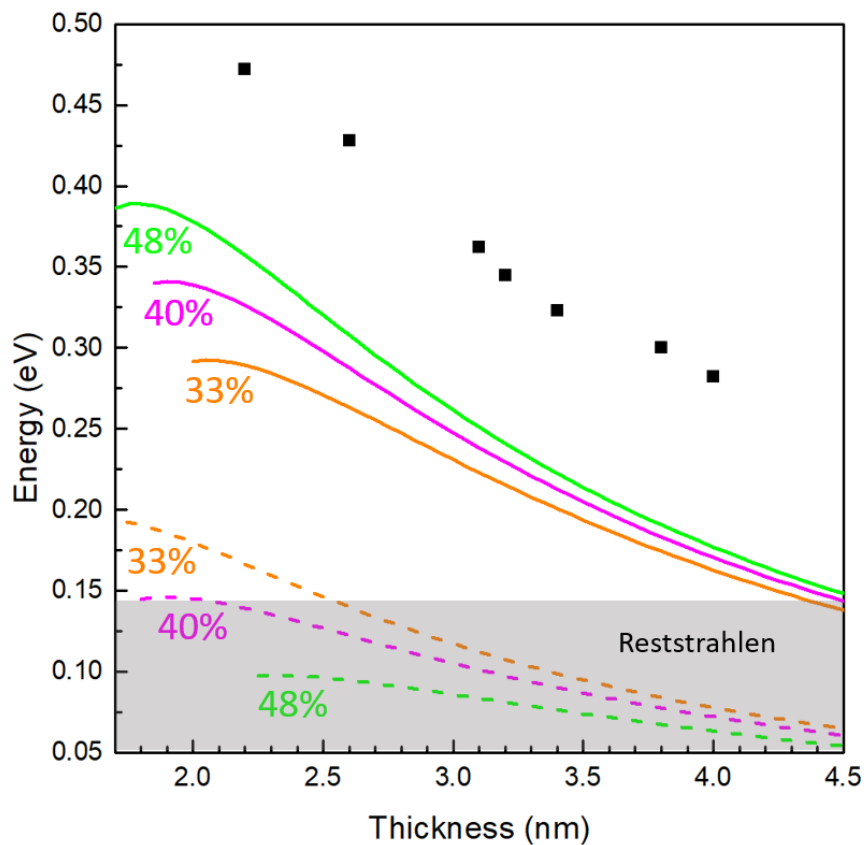


Figure S1: Calculated ISB energy versus well thickness for an Mg content in the barrier of 33% (orange curve), 40 % (purple curve) and 48% (green curve). The full lines correspond to conduction band and the dashed lines correspond to valence band. The full black squares are the experimental peak energies measured by PIA. The grey area represented the Reststrahlen band.

C) Excitonic binding energy calculation

The binding energy is defined as the difference in energy between the bottom of the electron-hole pair continuum and the lowest excitonic bound state.

Following the method in ref [10], this binding energy is obtained as an integral (over the coordinates of the electron and hole perpendicular to the confining layers) of a prescribed function multiplied by the squares of the electron and the hole subband envelope functions:

$$\Delta_{ij} = \int_{-\infty}^{+\infty} dz_e dz_h \left| \varphi_i^{(e)}(z_e) \right|^2 \left| \varphi_j^{(h)}(z_h) \right|^2 E_B^{(2D)}(z_e - z_h)$$

This function is obtained by neglecting both band nonparabolicity (arising from valence-conduction band coupling) and valence-band mixing. $\varphi_i^{(e)}$ ($\varphi_j^{(h)}$) is the conduction (valence) subband envelope function satisfying:

$$\left[-\frac{\hbar^2}{2} \frac{d}{dz_e} \left(\frac{1}{m_e} \frac{d}{dz_e} \right) + V_e(z_e) \right] \varphi_i^{(e)} = E_i^{(e)} \varphi_i^{(e)}(z_e)$$

and

$$\left[-\frac{\hbar^2}{2} \frac{d}{dz_h} \left(\frac{1}{m_h} \frac{d}{dz_h} \right) + V_h(z_h) \right] \varphi_j^{(h)} = E_j^{(h)} \varphi_j^{(h)}(z_h)$$

$E_i^{(e)}$ ($E_j^{(h)}$) is the electron (valence) subband-edge energies (energies at $k=0$) and where (i,j) = 1, 2, 3,... label the states in order of increasing energies. $E_B^{(2D)}(z_e - z_h)$ corresponds to the two-dimensional exciton energy and is the eigenvalue of the electron-hole pair H_{e-h} Hamiltonian:

$$H_{e-h} = -\frac{\hbar^2}{2} \frac{d}{dz_e} \left(\frac{1}{m_e} \frac{d}{dz_e} \right) - \frac{\hbar^2}{2} \frac{d}{dz_h} \left(\frac{1}{m_h} \frac{d}{dz_h} \right) + V_e(z_e) + V_h(z_h) - \frac{\hbar^2}{2\mu} \nabla^2 - \frac{e^2}{\epsilon|r_e - r_h|}$$

By choosing an electron-hole pair wave function with the following form:

$$\psi_n(r_e, r_h) = \phi(z_e, z_h) g_n(\rho, z_e - z_h)$$

with $n = 1, 2, \dots$ which labels eigenstates in order of increasing energy and g_n which represents a two-dimensional excitonic hamiltonian where the electron is confined the $z = z_e$ plane and the hole is confined in the $z = z_h$ and depending on $\rho = r_{e||} - r_{h||}$.

By using $Z = z_e - z_h$, $g_n(\rho, Z)$ behaves with the following the boundary conditions: $g_n(\rho, Z) \rightarrow 0$ as $\rho \rightarrow \infty$ and $g_n(0, Z)$ is bounded and is normalized as follows:

$$\int_0^\infty \rho d\rho |g_n(\rho, Z)|^2 = 1$$

The two-dimensional exciton energy $E_B^{(2D)}(Z)$ is then obtained by resolving the radial Schrödinger equation:

$$-\frac{\hbar^2}{2\mu} \frac{1}{\rho} \frac{d}{d\rho} \left(\rho \frac{dg_n(\rho, Z)}{d\rho} \right) - \frac{e^2}{\varepsilon(\rho^2 + Z^2)^{\frac{1}{2}}} g_n(\rho, Z) = -E_n^{2D}(Z) g_n(\rho, Z)$$

The exciton binding energy increases as the QW thickness decreases, and its dependence on subband number was approximated following the Leavitt-Little model [10] scaled with an effective exciton Bohr radius of 18.0 Å and an effective Rydberg energy of 60.8 meV derived from the electron and hole effective masses.

D) Influence of V-groove profile on quantum confinement

The fact that the X_1 - X_2 excitonic transition is not observed could be explained from the quasi-1D nature of this system, as we discuss in the following. Indeed, figure S2a presents a TEM picture for sample C as well as the amplitude of the wave-functions for the hh1, e1 and e2 states. The Mg concentration fluctuation is taken into account by placing a vertical 1 nm thick areas of $Zn_{67}Mg_{33}O$ ($Zn_{52}Mg_{48}O$) inside the $Zn_{60}Mg_{40}O$ barriers at the bottom (top) edges (Figure S2b). The angle between the $Zn_{60}Mg_{40}O$ barriers and the 3.1 nm thick ZnO QWs interfaces is $\sim 16^\circ$. These structural features are determined based on the TEM pictures. The Nextnano simulations [9] for this structure (figures S2.c,d and e) show wave-functions amplitudes of the confined states in the valence (hh1) and conduction bands (e1, e2) considering periodic conditions along the a and the m-axis.

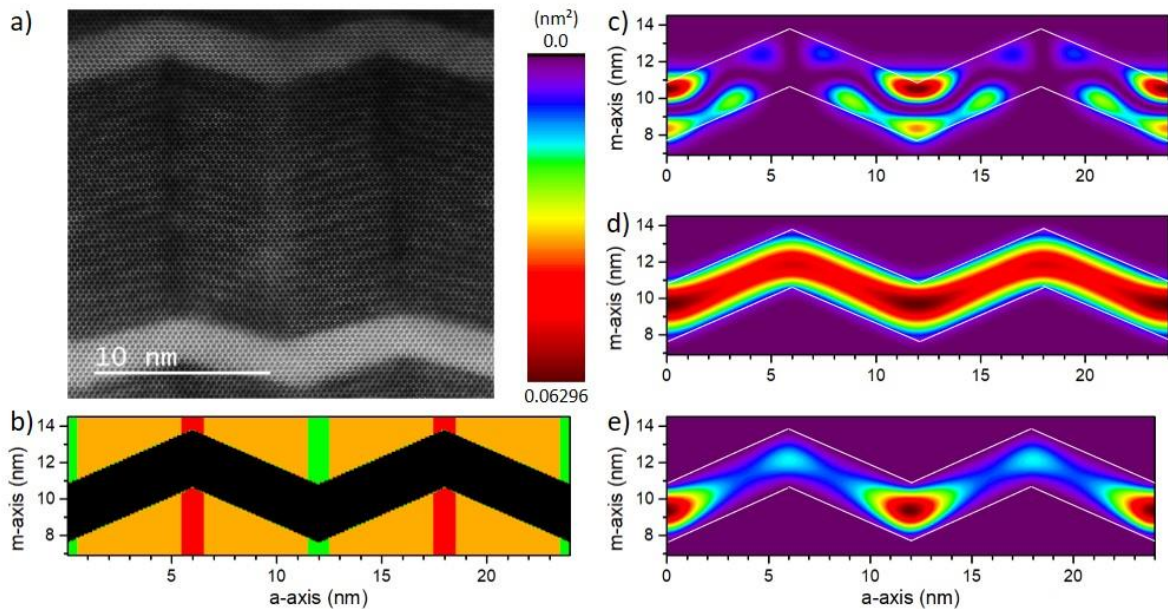


Figure S2: (a) TEM image of sample C, (b) alloy structure used for Schrödinger simulation with ZnO QW (black area), $Zn_{60}Mg_{40}O$ barrier (yellow area), $Zn_{52}Mg_{48}O$ barrier (red area), $Zn_{67}Mg_{33}O$ barrier (green area) and the amplitude of the e2 (c), e1 (d) and hh1 (e) wave-function.

This structure exhibits the wave-functions confinement in the vicinity of the bottom edges especially for the e2 state. Although the hh1 and e1 states spread along the QW layer, their wave-functions are mainly localized in bottom edges, while e2 state is completely confined in the vicinity of the bottom edges. So, this irregular profile of the QW layers and the compositional inhomogeneity of the $Zn_{1-x}Mg_xO$ barriers transforms the density of state (DOS) of free-carriers in the second subband from 2D (QW) to quasi-1D systems (quantum wire). The DOS correspondingly evolves from a plateau (2D) to a divergent peak (1D) at the continuum edge (variation on $1/\sqrt{E - e2}$). The 1D divergence is nevertheless known to be very sensitive to disorder effects, and hard to observe. Instead, the inhomogeneous disorder broadens the latter, and introduces a strong and broad X1-to-e2 transition peak that eventually hidden the much less intense X1-X2 absorption. Besides, we have checked that the V-groove profile of the QW layers and the Mg concentration fluctuation of the barriers have a negligible redshifted influence on the interband and ISB transition energies (< 10 meV).

E) Miscellaneous exciton transitions.

The Reststrahlen band of ZnO material is between 51 et 146 meV. The ionization of the X1 exciton into e1 is allowed by an energy given by the binding energy of the X1 exciton ($E_{X1-e1} = \Delta_1$). In our case, the transition X1-e1 involves energy between 92.4 and 108.4 meV. Therefore, these transitions are lying into the Reststrahlen band of the ZnO material and they cannot be detectable.

Concerning the transition between the hh1-e1 and the hh2-e2 states, the selection rules forbid this type of transition.

F) Inhibition of the X1-X2 inter-exciton transition.

The dipole matrix element for the X1 → X2 transition writes:

$$\langle \Psi_{X1} | z | \Psi_{X2} \rangle = \iiint dx dy dz \Psi_{X1}^*(\vec{r}) z \Psi_{X2}(\vec{r})$$

$$\Psi_{X1}(\vec{r}) \approx \phi_{E1}(y, z) \chi_{H1}(y, z) F_1(x, y)$$

$$\Psi_{X2}(\vec{r}) \approx \phi_{E2}(y, z) \chi_{H1}(y, z) F_2(x)$$

where $\rho = \sqrt{x^2 + y^2}$, z is taken along the m -axis and y along the a -axis. The amplitudes in figure S2 c,d,e correspond respectively to $|\phi_{E2}(y, z)|^2$, $|\phi_{E1}(y, z)|^2$ and $|\chi_{H1}(y, z)|^2$. Figure S2 shows a much stronger confinement along the a -axis for the $e2$ state, as compared to the $e1$ and $hh1$ ones. One approximates correspondingly:

$$\Psi_{X1}(\vec{r}) \approx \varphi_{E1}(z) \chi_{H1}(z) F_1(\rho) : \text{quasi} - 2D$$

$$\Psi_{X2}(\vec{r}) \approx \varphi_{E2}(z) \chi_{H1}(z) G_{E2}(y) F_2(x) : \text{quasi} - 1D$$

and thus (discarding the identical z -related term):

$$\langle \Psi_{X1} | \Psi_{X2} \rangle \propto \iint dx dy G_{E2}(y) F_2(x) F_1(\rho)$$

In the extreme 2D and 1D limits one has:

$$F_1(\rho) \approx F_1^{(2D)}(\rho) = N_1 \exp \{-\rho/\lambda_1\} : \text{ground 2D state}$$

$$F_2(x) \approx F_2^{(1D)}(x) = N_2 x \exp \{-|x|/\lambda_2\} : \text{ground 1D state}$$

where N are normalisation constants and λ_n effective Bohr radii. The fact that the ground exciton envelope $F_2^{(1D)}(x)$ has a p-like shape (and thus vanishes at $x=0$) is due to the strong divergence of the Coulomb potential at 1D. In this case the X1-to-X2 absorption vanishes exactly (by symmetry). Note that for a “standard” QW the envelopes of the ground excitons related to the e1 and e2 subbands would both display a quasi-2D dependence $\propto \exp\{-\rho/\lambda\}$, and, for similar binding energies their overlap would be near unity. The wavefunction amplitudes in figure S2 indicates a strong but not extreme 1D behaviour for the e2 state, so that the matrix element does not exactly vanishes in our structure, but is expected to be much smaller than for “standard” QWs.

These two effects add their contributions and help understanding why exciton-to-exciton dominates the photo-induced absorption in GaAs-based samples but are sizeably inhibited in our samples. A more detailed evaluation of the ISB spectrum (beyond the scope of this work) should be carefully taken into account such dimensionality effects.

References:

- [1] B. Laumer, F. Schuster, M. Stutzmann, A. Bergmaier, J. Appl. Phys. 113, 233512 (2013).
- [2] S.-H. Jang and S. F. Chichibu, J. Appl. Phys. 112, 073503 (2012).
- [3] J. Chen, W. Z. Shen, N. B. Chen, D. J. Qui, H. Z. Wu, J. Phys: Condens Matter 15, L475 (2003).
- [4] C. Franz, Materials research, Volume 1494, Cambridge University Press (2013).
- [5] Y.-N. Xu et W. Y. Ching, PRB 43, 4461 (1991).
- [6] H. Yin, J. Chen, Y. Wang, J. Wang and H. Guo, Scientific Reports 7, 41567 (2017).
- [7] A.R. Denton and N.W Ashcroft, Phys. Rev. A 43 (6), 3161-3164 (1991).
- [8] T. C. Damen, S. P. S. Porto, B. Tell, Phys. Rev. B **142**, 570 (1966).
- [9] Nextnano3 software, <http://www.nextnano.de>.

[10] R. P. Leavitt and J. W. Little, Phys. Rev. B 42, 11774 (1990).